

# High temperature promoted synthesis of graphitic carbon nitride with porous structure and enhanced photocatalytic activity

Lei Shi<sup>2</sup> · Tao Liang<sup>2</sup> · Lin Liang<sup>3</sup> · Fangxiao Wang<sup>2</sup> · Mengshuai Liu<sup>2</sup> · Jianmin Sun<sup>1,2</sup>

Published online: 12 July 2015

© Springer Science+Business Media New York 2015

**Abstract** Graphitic carbon nitride (g-C<sub>3</sub>N<sub>4</sub>) was prepared by the polycondensation of melamine at 650 °C for 2 h, then thoroughly characterized by X-ray diffraction, Fourier transform infrared spectroscopy, X-ray photoelectron spectroscopy, elemental analysis, transmission electron microscopy, N<sub>2</sub> adsorption–desorption isotherms, UV–Vis diffuse reflectance spectra and photoluminescence spectra. The photocatalytic activity of g-C<sub>3</sub>N<sub>4</sub> catalyst was evaluated by the degradation of Rhodamine B, Methylene blue and phenol solution under visible-light irradiation, which showed that g-C<sub>3</sub>N<sub>4</sub> calcined at 650 °C increased the degree of condensation, thus led to the decreased band gap and exhibited better photocatalytic activity than the reference sample treated at 520 °C and P25. The integrated positive effects of porous structure, larger surface area, stronger visible-light absorption and higher separation efficiency for photoinduced electron–hole pairs over g-C<sub>3</sub>N<sub>4</sub> treated at 650 °C resulted in its improved photocatalytic activity for degrading pollutants. Additionally, the as-prepared g-C<sub>3</sub>N<sub>4</sub> possessed good structural and catalytic stability after three recycles.

**Keywords** Graphitic carbon nitride · Higher temperature · Photocatalyst · Porous structure · Visible light · Dye

## 1 Introduction

Recently, semiconductor photocatalysis technology has drawn much attention due to their promising applications in environmental purification and solar energy conversion [1–4]. Besides the traditional photocatalyst star of TiO<sub>2</sub>, a great many photocatalysts with enhanced efficiency were developed, such as ZnO [5], Co<sub>3</sub>O<sub>4</sub> [6], CdS [7], Ag<sub>3</sub>PO<sub>4</sub> [8], AgX (X = Cl, Br, I) [9–11], BiOX (X = Cl, Br, I) [12–14] and BiPO<sub>4</sub> [15].

As visible light driven metal-free photocatalyst, Wang et al. [16] first reported graphitic carbon nitride (g-C<sub>3</sub>N<sub>4</sub>) in 2009. With the narrow optical band gap of 2.7 eV, g-C<sub>3</sub>N<sub>4</sub> possessed the high catalytic performance for hydrogen production via water splitting [17, 18] and degradation of organic pollutants under visible light irradiation [19–23]. Although g-C<sub>3</sub>N<sub>4</sub> exhibited an attractive candidate photocatalyst, the existed problems such as high recombination rate of the photogenerated electron–hole pairs, the absorbance of only blue light up to 460 nm and the low specific surface area, limited the efficient utilization of solar energy and led to the poor photocatalytic efficiency. In order to overcome the disadvantages, some strategies such as non-metal doping [24], noble metal deposition [25], coupling with semiconductor composite [26–28] and morphology control [29, 30], have been exploited to enhance its activity. In addition, it was reported that increasing heat treatment temperature was alternative effective method to improve the photocatalytic activity of g-C<sub>3</sub>N<sub>4</sub>. Niu et al. [31] prepared g-C<sub>3</sub>N<sub>4</sub> by the polycondensation of

---

Lei Shi and Tao Liang have contributed equally to this study.

✉ Jianmin Sun  
sunjm@hit.edu.cn

<sup>1</sup> State Key Laboratory of Urban Water Resource and Environment, Harbin Institute of Technology, Harbin 150080, China

<sup>2</sup> The Academy of Fundamental and Interdisciplinary Science, Harbin Institute of Technology, Harbin 150080, China

<sup>3</sup> School of Life Science and Technology, Harbin Institute of Technology, Harbin 150080, China

dicyandiamide precursor at 600 °C, which exhibited better visible light catalytic activity for hydrogen production and degrading organic pollutant than g-C<sub>3</sub>N<sub>4</sub> treated at 550 °C. Long et al. [32] fabricated g-C<sub>3</sub>N<sub>4</sub> by thermal-induced desulfurization then polymerization of guanidine thiocyanate at 700 °C, which displayed seven times larger for photocatalytic hydrogen evolution than the reference sample polymerized at 550 °C.

In this manuscript, g-C<sub>3</sub>N<sub>4</sub> was prepared by the polycondensation of melamine precursor at 650 °C for 2 h, and its morphology and optical property were well characterized. Compared with the reference sample obtained by heating melamine at 520 °C, the as-prepared g-C<sub>3</sub>N<sub>4</sub> treated at 650 °C possessed porous structure, larger surface area, stronger visible-light absorption and higher separation efficiency for photoinduced electron–hole pairs. These positive factors resulted in its enhanced photodegradation activity of Rhodamine B (RhB), Methylene blue (MB) and phenol under visible light. Moreover, the high temperature treated g-C<sub>3</sub>N<sub>4</sub> still kept structural and catalytic stability after three recycles.

## 2 Experimental

### 2.1 The preparation of samples

3 g of melamine was placed in a crucible with a cover and heated at 650 °C for 2 h at the heating rate of 4 °C min<sup>-1</sup> to obtain orange g-C<sub>3</sub>N<sub>4</sub>, which was denoted as g-C<sub>3</sub>N<sub>4</sub>(650). For comparison, g-C<sub>3</sub>N<sub>4</sub> was prepared in the same way only at different polycondensation temperature [33]. In the typical run, 3 g melamine was placed in a crucible with a cover, and heated at 500 °C for 2 h then 520 °C for 2 h to obtain light yellow g-C<sub>3</sub>N<sub>4</sub>, denoted as g-C<sub>3</sub>N<sub>4</sub>(520).

### 2.2 Characterizations

X-ray diffraction (XRD) was carried out on a Bruker D8 Advance X-ray powder diffractometer with Cu K $\alpha$  radiation (40 kV, 30 mA) for phase identification. Fourier transform infrared spectroscopy (FTIR) were recorded within 400–4000 cm<sup>-1</sup> on Perkin Elmer spectrum 100 using KBr discs. X-ray photoelectron spectroscopy (XPS) were recorded on Thermo Fisher Scientific Escalab 250Xi. The morphology and particle size of the product were examined by a transmission electron microscopy (TEM, Tecnai G2 Spirit). N<sub>2</sub> adsorption–desorption isotherms were collected at 77 K using a Quantachrome NOVA 2000 surface area and porosity analyzer. Samples were outgassed at 150 °C for 12 h prior to measurements. The UV–Vis diffuse reflectance spectra (DRS) were measured by

Perkin Elmer Lambda 750 UV–Vis spectrometer. Elemental analyses (EA) for the carbon and nitrogen contents were performed on a Vario Elcube CHN analyzer. The photoluminescence spectra (PL) were obtained by a Perkin Elmer LS55 spectrometer with the excitation wavelength of 325 nm.

### 2.3 Photocatalytic test

The photocatalytic performance of the samples was evaluated through degradation of RhB, MB and phenol. The visible light was provided by 300 W Xe arc lamp with cut off filter ( $\lambda > 400$  nm). 0.1 g photocatalyst was dispersed into 100 mL 5 mg L<sup>-1</sup> pollutant solution under magnetic stirring. Prior to the light irradiation, the dispersion was kept in dark for 60 min under stirring to reach the adsorption–desorption equilibrium. Then the solution was collected at given time interval and centrifuged to remove the catalyst, then analyzed on UV–Vis spectrometer. For comparison, the photodegraded reactions were also carried out in the absence of any catalyst and in the presence of P25. The degradation efficiency was calculated by  $C/C_0$ , where  $C$  is the concentration of remaining pollutant solution at each time interval, while  $C_0$  is the initial concentration.

## 3 Results and discussion

Figure 1 shows the XRD patterns of reference g-C<sub>3</sub>N<sub>4</sub>(520) and as-prepared g-C<sub>3</sub>N<sub>4</sub>(650). As shown, typical g-C<sub>3</sub>N<sub>4</sub> structures were detected and no impurity phase was found. The main peaks observed around at 27.4° and 13.1° were indexed to (002) and (100) planes of hexagonal g-C<sub>3</sub>N<sub>4</sub> (JCPDS card no. 87-1526), respectively corresponding to

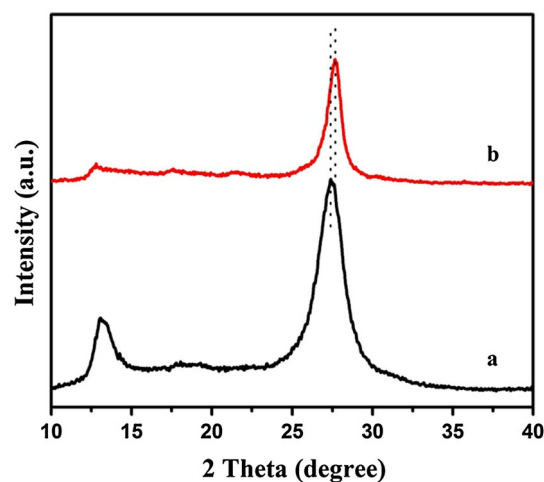
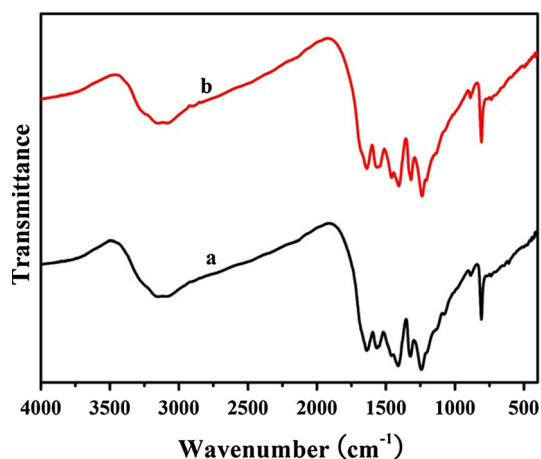


Fig. 1 XRD patterns of (a) g-C<sub>3</sub>N<sub>4</sub>(520) and (b) g-C<sub>3</sub>N<sub>4</sub>(650)

the graphite-like stacking and the in-plane structural repeating motifs in the conjugated aromatic units of  $g\text{-C}_3\text{N}_4$ . Whereas, the former peak of  $g\text{-C}_3\text{N}_4(650)$  shifted slightly from  $27.4^\circ$  to  $27.6^\circ$ , corresponding to a decrease in the interlayer stacking distance from 0.325 to 0.323 nm. This result suggested that the degree of condensation of  $g\text{-C}_3\text{N}_4(650)$  was improved at higher temperature, in another word, the gallery distance between the basic sheets was decreased when melamine was treated at higher temperature. Moreover, the intensity of other peak at  $13.1^\circ$  became weakened for  $g\text{-C}_3\text{N}_4(650)$ , indicating that long-range order of the in-plane structural packing in the  $g\text{-C}_3\text{N}_4$  sheets was reduced [31].

FTIR spectra of  $g\text{-C}_3\text{N}_4(520)$  and  $g\text{-C}_3\text{N}_4(650)$  were shown in Fig. 2. Both of samples exhibited the typical IR patterns of graphitic carbon nitride. The absorption peak at  $808\text{ cm}^{-1}$  was considered as the out-of-plane skeletal bending modes of triazine [20]. The broad bands in  $3000\text{--}3500\text{ cm}^{-1}$  region could be attributed to the adsorbed O–H bands and N–H components [32]. The absorption



**Fig. 2** FTIR spectra of (a)  $g\text{-C}_3\text{N}_4(520)$  and (b)  $g\text{-C}_3\text{N}_4(650)$

bands in the range of  $1200\text{--}1700\text{ cm}^{-1}$  were assigned to the typical stretching modes of  $\text{C}_3\text{N}_4$  heterocycles [34].

XPS spectra of  $g\text{-C}_3\text{N}_4(650)$  was investigated in Fig. 3. In C 1s spectra, two peaks could be distinguished to be centered at 284.6 and 288.1 eV. The peak at 284.6 eV was exclusively assigned to carbon atoms (C–C bonding) originating from the carbon-containing contamination, and the peak at 288.1 eV was regarded as  $\text{sp}^2\text{ C}=\text{N}$  bond [21]. N 1s spectrum (Fig. 3B) was divided into three peaks at 398.6, 399.6 and 400.8 eV, which were assigned to N atom  $\text{sp}^2$ -bonded to two carbon atoms (C–N=C), tertiary nitrogen (N–(C)<sub>3</sub>) and amino functional groups with a hydrogen atom (N–H) [35], respectively. Simultaneously, elemental analysis indicated that the atom ratio of carbon to nitrogen for  $g\text{-C}_3\text{N}_4(520)$  and  $g\text{-C}_3\text{N}_4(650)$  was respective at 0.647 and 0.666. The both C/N ratios were lower than 0.75 for the ideal crystal  $g\text{-C}_3\text{N}_4$ , which revealed the existence of the amino groups, consistent with the FTIR and XPS results. The amino groups were originated from the incomplete condensation of melamine, indeed, the residual hydrogen atoms bonded to the edges of the graphene-like C–N sheet in the form of C–NH<sub>2</sub> and 2C–NH bonds [33].

TEM images for  $g\text{-C}_3\text{N}_4(520)$  and  $g\text{-C}_3\text{N}_4(650)$  were shown in Fig. 4. The reference  $g\text{-C}_3\text{N}_4$  displayed aggregated layers and irregular shapes, but the smooth and flat layers were clearly seen in Fig. 4A. Although  $g\text{-C}_3\text{N}_4(650)$  also showed irregular shapes with aggregated structures, many irregular holes were clearly observed (Fig. 4B), which might be attributed to the decomposition of partial location on the  $g\text{-C}_3\text{N}_4(650)$  surface during higher temperature thermal treatment.

Simultaneously, the N<sub>2</sub> adsorption–desorption isotherms of the as-prepared  $g\text{-C}_3\text{N}_4(520)$  and  $g\text{-C}_3\text{N}_4(650)$  samples were displayed in Fig. 5A. Compared with  $g\text{-C}_3\text{N}_4(520)$ ,  $g\text{-C}_3\text{N}_4(650)$  sample exhibited type IV isotherm, which was characteristic of porous materials. Correspondingly, the BJH pore size distributions further confirmed the formation of pores in Fig. 5B. And the pore width of as-

**Fig. 3** XPS spectra of  $g\text{-C}_3\text{N}_4(650)$  sample: **A** C 1s and **B** N 1s

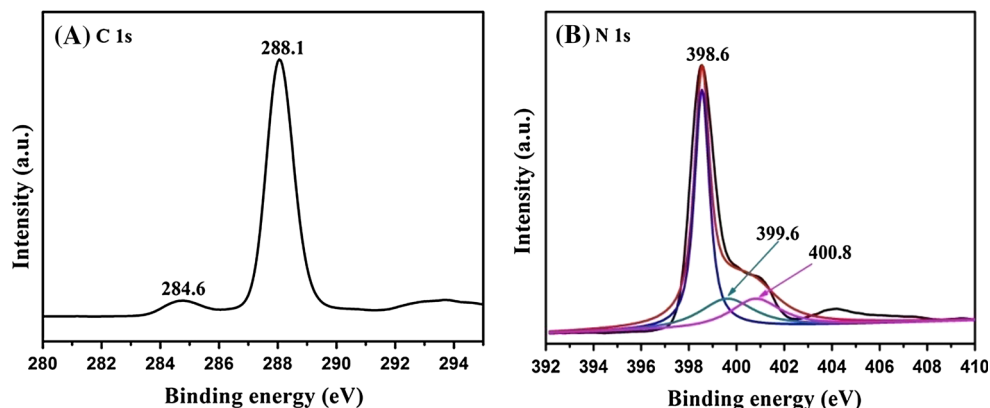


**Fig. 4** TEM images of **A** g-C<sub>3</sub>N<sub>4</sub>(520) and **B** g-C<sub>3</sub>N<sub>4</sub>(650)

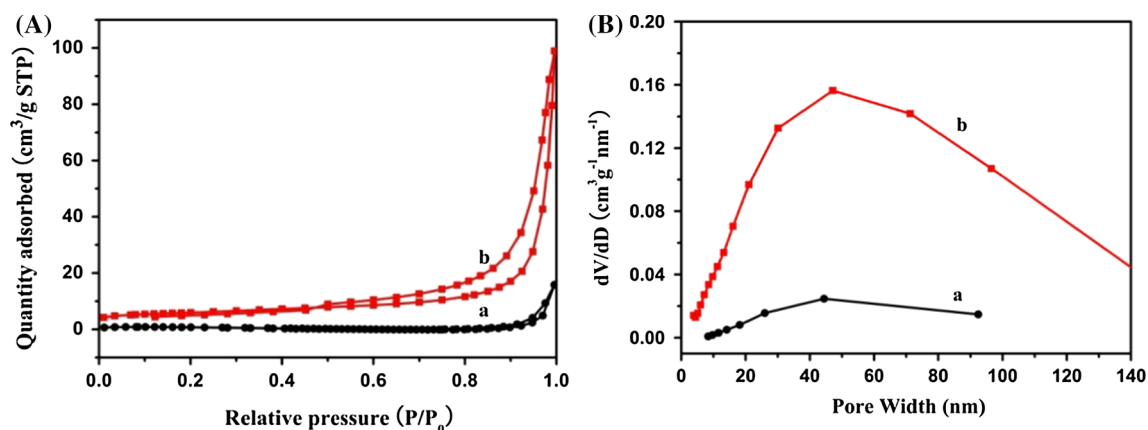
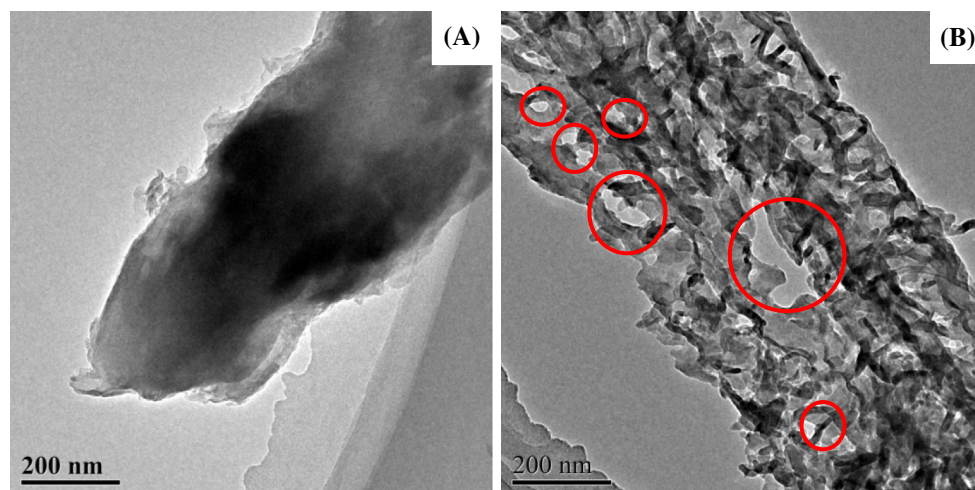
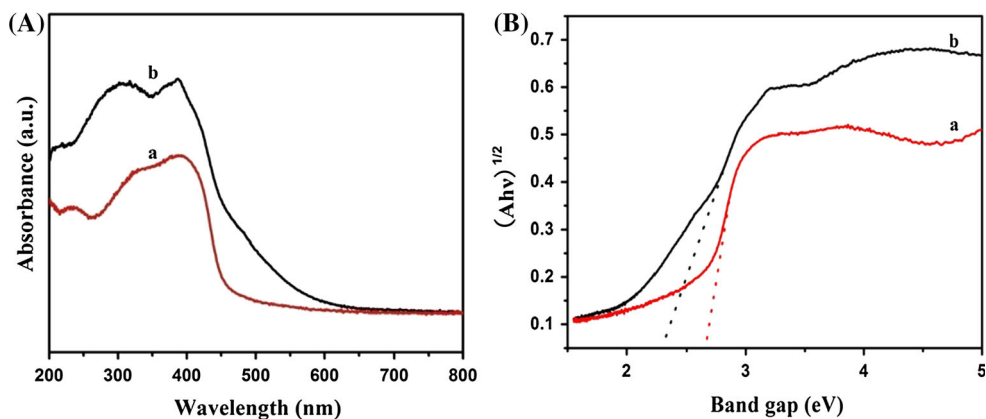


**Fig. 5** **A** N<sub>2</sub> adsorption–desorption isotherms and **B** pore size distributions of (a) g-C<sub>3</sub>N<sub>4</sub>(520) and (b) g-C<sub>3</sub>N<sub>4</sub>(650)

**Fig. 6** **A** UV–vis absorption spectra and **B** Plots of  $(Ah\nu)^{1/2}$  versus energy ( $h\nu$ ) for the band gap energy of (a) g-C<sub>3</sub>N<sub>4</sub>(520) and (b) g-C<sub>3</sub>N<sub>4</sub>(650)



prepared g-C<sub>3</sub>N<sub>4</sub>(650) was in the range of 20–100 nm, which was consistent with the result of TEM. BET surface areas of g-C<sub>3</sub>N<sub>4</sub>(520) and g-C<sub>3</sub>N<sub>4</sub>(650) were 2.4 and 16.3 m<sup>2</sup> g<sup>-1</sup>, respectively. The increased surface areas and the existed pores could provide more active sites for

surface reaction and facilitate electrons transfer, thus g-C<sub>3</sub>N<sub>4</sub>(650) would give rise to the higher photocatalytic activity for the degradation of pollutants than g-C<sub>3</sub>N<sub>4</sub>(520).

The optical properties of the samples were investigated by DRS in Fig. 6A. It was observed that the absorption of

g-C<sub>3</sub>N<sub>4</sub>(650) was stronger than g-C<sub>3</sub>N<sub>4</sub>(520) from UV light to visible light, which was in agreement with the color change from yellow g-C<sub>3</sub>N<sub>4</sub>(520) to orange g-C<sub>3</sub>N<sub>4</sub>(650).

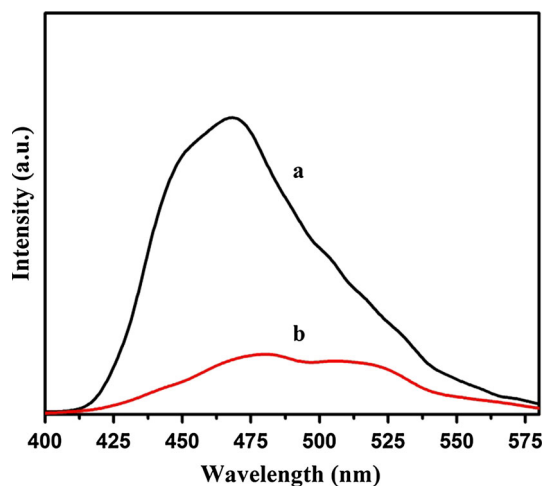


**Fig. 7** Photoluminescence spectra of (a) g-C<sub>3</sub>N<sub>4</sub>(520) and (b) g-C<sub>3</sub>N<sub>4</sub>(650)

In order to estimate the optical band gaps for the samples, the intercept of the tangents to the plots of  $(Ah\nu)^{1/2}$  versus photon energy was carried out as shown in Fig. 6B [36, 37]. The band gaps of g-C<sub>3</sub>N<sub>4</sub>(520) and g-C<sub>3</sub>N<sub>4</sub>(650) were determined to be 2.66 and 2.30 eV. Thanks to the narrowed band gap, a more efficient utilization of solar energy could be achieved, thus the improved photocatalytic activity of g-C<sub>3</sub>N<sub>4</sub>(650) would be anticipated.

PL emission spectrum originated from the recombination of free charge carriers usually serves as a good candidate for the characterization the charge migration, transfer and separation of semiconductors. In Fig. 7, the remarkably reduced intensity over g-C<sub>3</sub>N<sub>4</sub>(650) were observed compared with g-C<sub>3</sub>N<sub>4</sub>(520), which indicated that the recombination rates for photoinduced electron–hole pairs were reduced over g-C<sub>3</sub>N<sub>4</sub>(650). The improved separation efficiency was resulted from the more efficient electron relocalization on surface terminal sites, porous structure and larger surface area [18, 34], thus favoring the photocatalytic activity.

To investigate the photocatalytic activity, the photodegradation of RhB was carried out under visible light

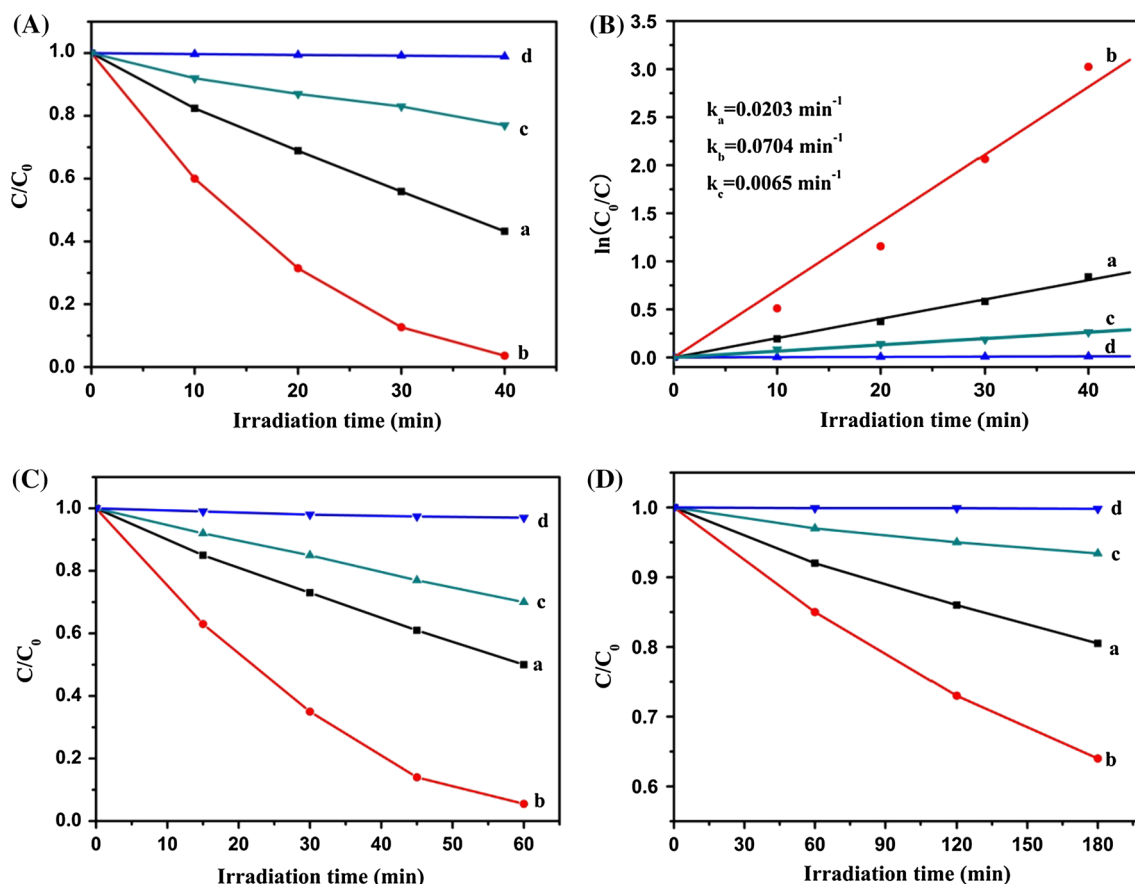


**Fig. 8** A Degradation rates of RhB, B First-order kinetic plots, C Degradation rates of MB and D Degradation rates of phenol over (a) g-C<sub>3</sub>N<sub>4</sub>(520), (b) g-C<sub>3</sub>N<sub>4</sub>(650), (c) P25 TiO<sub>2</sub> and (d) blank



irradiation. As shown in Fig. 8A,  $g\text{-C}_3\text{N}_4(520)$  and P25  $\text{TiO}_2$  exhibited moderate photocatalytic activity, only 55 and 23 % RhB was degraded after 40 min, while almost 100 % RhB was photodegraded under the same conditions over  $g\text{-C}_3\text{N}_4(650)$ . To have a better understanding of the reaction kinetics of RhB degradation, Fig. 8B shows a linear relationship between  $\ln(C_0/C)$  and the irradiation time ( $t$ ). As the relationships were linear ( $R \geq 0.99$ ), the photocatalytic degradation curves in all cases fit well with pseudo-first-order kinetics.  $g\text{-C}_3\text{N}_4(650)$  displayed the enhanced rate constants of  $0.0704 \text{ min}^{-1}$ , which was approximately 3.5 times larger than  $0.0203 \text{ min}^{-1}$  over  $g\text{-C}_3\text{N}_4(520)$  and 10.5 times larger than  $0.0065 \text{ min}^{-1}$  over P25  $\text{TiO}_2$ . Furthermore, the photodegradation of MB and phenol was also investigated. As shown from Fig. 8C, MB could be almost degraded within 60 min by  $g\text{-C}_3\text{N}_4(650)$ , while only 50 and 30 % MB was degraded by  $g\text{-C}_3\text{N}_4(520)$  and P25, respectively. In Fig. 8D, the degraded result of

phenol was similar with those of RhB and MB.  $g\text{-C}_3\text{N}_4(650)$  still exhibited better photocatalytic activity for degrading phenol than  $g\text{-C}_3\text{N}_4(520)$  and P25 under the same conditions.

Above results revealed that as-prepared  $g\text{-C}_3\text{N}_4(650)$  exhibited improved photocatalytic activities than  $g\text{-C}_3\text{N}_4(520)$ , which was explained by the following integrated effects. Firstly, compared with  $g\text{-C}_3\text{N}_4(520)$ ,  $g\text{-C}_3\text{N}_4(650)$  with porous structure possessed larger surface area, which could enhance the adsorption capacity to the pollutant and supply more catalytic active sites, accelerating the photocatalysis rate. Secondly,  $g\text{-C}_3\text{N}_4(650)$  displayed narrower bandgap and collected stronger absorption of visible light than  $g\text{-C}_3\text{N}_4(520)$ , which could utilize more energy of the light and tended to possess higher photocatalytic ability. Thirdly,  $g\text{-C}_3\text{N}_4(650)$  possessed higher separation efficiency for photoinduced electron–hole pairs than  $g\text{-C}_3\text{N}_4(520)$ . As a result, these positive effects endowed  $g\text{-C}_3\text{N}_4(650)$  superior photocatalytic performance.

In addition, the recycling experiments were repeated up to three times through decomposing RhB over  $g\text{-C}_3\text{N}_4(650)$ . After RhB was photodegraded in 40 min, the separated photocatalyst was washed with deionized water and ethanol, then dried at  $60^\circ\text{C}$  for 12 h and directly used for the next run. The photocatalytic activity of  $g\text{-C}_3\text{N}_4(650)$  after three cycles almost did not change (Fig. 9), suggesting that  $g\text{-C}_3\text{N}_4(650)$  was not photocorroded during the photodegradation process and kept good catalytic stability.

Moreover,  $g\text{-C}_3\text{N}_4(650)$  samples before and after photodegradation were also characterized by XRD and FTIR in Fig. 10. After three recycles, the unchanged XRD peaks at  $27.6^\circ$  and  $13.1^\circ$  indicated that the photocatalyst structure was stable (Fig. 10A). The same FTIR patterns of  $g\text{-C}_3\text{N}_4(650)$  sample before and after degradation (Fig. 10B) further proved the stability of  $g\text{-C}_3\text{N}_4(650)$ .

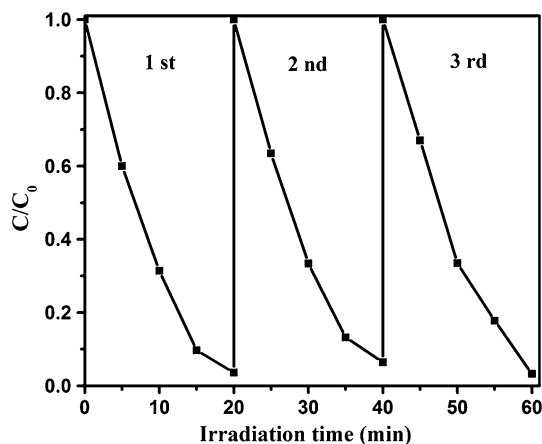
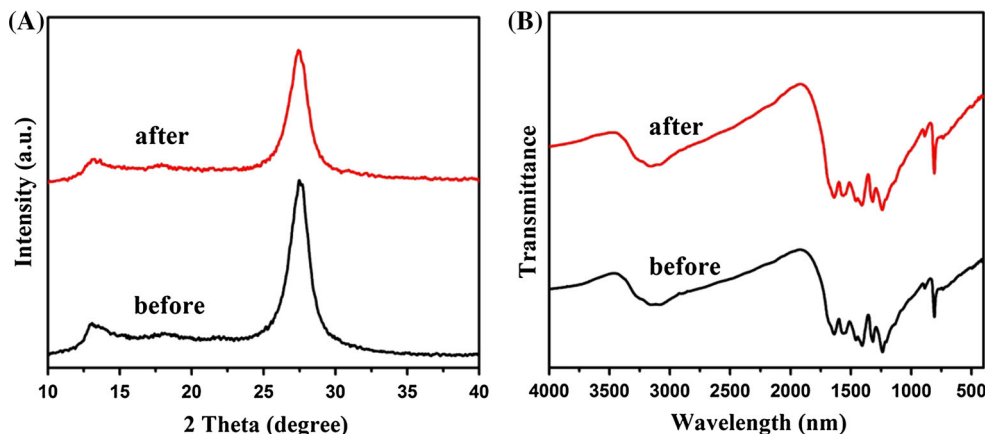


**Fig. 9** Recycling runs in the photodegradation of RhB over  $g\text{-C}_3\text{N}_4(650)$

**Fig. 10** A XRD patterns and B FTIR of  $g\text{-C}_3\text{N}_4(650)$  before and after three photocatalytic recycles



## 4 Conclusion

g-C<sub>3</sub>N<sub>4</sub>(650) was facily prepared by the polycondensation of melamine at higher temperature of 650 °C. Compared with the reference sample treated at 520 °C, g-C<sub>3</sub>N<sub>4</sub>(650) condensed at higher temperature exhibited porous structure, the larger surface area, stronger visible-light absorption and higher separation efficiency for photoinduced electrons and holes. The above integrated positive effects resulted in the remarkable enhancement of the photocatalytic activity for degrading RhB, MB and phenol. Moreover, g-C<sub>3</sub>N<sub>4</sub>(650) still kept the excellent stability after three recycles. The present contribution exhibited that high temperature treatment was a facile and efficient route for tuning the degree of condensation and altering the textural structure of conjugated g-C<sub>3</sub>N<sub>4</sub> polymers, which would be a promising star for pollutant abatement and clean energy.

**Acknowledgments** We sincerely acknowledge the financial supports from National Natural Science Foundation of China (21373069), Science Foundation of Harbin City (NJ20140037), State Key Lab of Urban Water Resource and Environment of Harbin Institute of Technology (HIT2015DX08) and the Fundamental Research Funds for the Central Universities (HIT. IBRSEM. 201327).

## References

1. X. Chen, L. Liu, P.Y. Yu, S.S. Mao, *Science* **331**, 746 (2011)
2. R. Asahi, T. Morikawa, T. Ohwaki, K. Aoki, Y. Taga, *Science* **293**, 269 (2001)
3. L. Shi, L. Liang, J. Ma, J.M. Sun, *Superlattice Microstruct.* **62**, 128 (2013)
4. J.H. Park, S. Kim, A.J. Bard, *Nano Lett.* **6**, 24 (2006)
5. E.S. Jang, J.H. Won, S.J. Hwang, J.H. Choy, *Adv. Mater.* **18**, 3309 (2006)
6. Y. Dong, K. He, L. Yin, A. Zhang, *Nanotechnology* **18**, 435602 (2007)
7. F. Yang, N. Yan, S. Huang, Q. Sun, L. Zhang, Y. Yu, *J. Phys. Chem. C* **116**, 9078 (2012)
8. Y. Bi, S. Ouyang, N. Umezawa, J. Cao, J. Ye, *J. Am. Chem. Soc.* **133**, 6490 (2011)
9. P. Wang, B. Huang, X. Qin, X. Zhang, Y. Dai, J. Wei, M. Whangbo, *Angew. Chem. Int. Ed.* **47**, 7931 (2008)
10. D. Wang, Y. Duan, Q. Luo, X. Li, L. Bao, *Desalination* **270**, 174 (2011)
11. H. Yu, L. Liu, X. Wang, P. Wang, J. Yu, Y. Wang, *Dalton Trans.* **41**, 10405 (2012)
12. L. Zhang, W. Wang, L. Zhou, M. Shang, S. Sun, *Appl. Catal. B Environ.* **90**, 458 (2009)
13. H. Cheng, B. Huang, P. Wang, Z. Wang, Z. Lou, J. Wang, X. Qin, X. Zhang, Y. Dai, *Chem. Commun.* **47**, 7054 (2011)
14. X. Xiao, W.D. Zhang, *J. Mater. Chem.* **20**, 5866 (2010)
15. C. Pan, J. Xu, Y. Wang, D. Li, Y. Zhu, *Adv. Funct. Mater.* **22**, 1518 (2012)
16. X.C. Wang, K. Maeda, A. Thomas, K. Takanebe, G. Xin, J.M. Carlsson, K. Domenet, M. Antonietti, *Nat. Mater.* **8**, 76 (2009)
17. A. Suryawanshi, P. Dhanasekaran, D. Mhamane, S. Kelkar, S. Patil, N. Gupta, S. Ogale, *Int. J. Hydrogen Energy* **37**, 9584 (2012)
18. X. Wang, K. Maeda, X. Chen, K. Takanebe, K. Domen, Y. Hou, X. Fu, M. Antonietti, *J. Am. Chem. Soc.* **131**, 1680 (2009)
19. L. Shi, L. Liang, J. Ma, F.X. Wang, J.M. Sun, *Dalton Trans.* **43**, 7236 (2014)
20. Y. Yang, Y. Guo, F. Liu, X. Yuan, Y. Guo, S. Zhang, W. Guo, M. Huo, *Appl. Catal. B Environ.* **142–143**, 828 (2013)
21. H. Xu, J. Yan, Y. Xu, Y. Song, H. Li, J. Xia, C. Huang, H. Wan, *Appl. Catal. B Environ.* **129**, 182 (2013)
22. S.C. Lee, H.O. Lintang, L. Yuliati, *Chem. Asian J.* **7**, 2139 (2012)
23. S. Ye, L.G. Qiu, Y.P. Yuan, Y.J. Zhu, J. Xia, J.F. Zhu, *J. Mater. Chem. A* **1**, 3008 (2013)
24. Z. Lin, X.C. Wang, *ChemSusChem* **7**, 1547 (2014)
25. L. Ge, C.C. Han, J. Liu, Y.F. Li, *Appl. Catal. A Gen.* **409–410**, 215 (2011)
26. L. Shi, L. Liang, J. Ma, F.X. Wang, J.M. Sun, *Catal. Sci. Technol.* **4**, 758 (2014)
27. J. Fu, B. Chang, Y. Tian, F. Xi, X. Dong, *J. Mater. Chem. A* **1**, 3083 (2013)
28. L. Shi, L. Liang, F.X. Wang, M.S. Liu, J.M. Sun, *J. Mater. Sci.* **50**, 1718 (2015)
29. M. Tahir, C. Cao, F.K. Butt, F. Idrees, N. Mahmood, Z. Ali, I. Aslam, M. Tanveer, M. Rizwan, T. Mahmood, *J. Mater. Chem. A* **1**, 13949 (2013)
30. J. Zhang, M. Zhang, C. Yang, X. Wang, *Adv. Mater.* **26**, 4121 (2014)
31. P. Niu, G. Liu, H.M. Cheng, *J. Phys. Chem. C* **116**, 11013 (2012)
32. B. Long, J. Lin, X. Wang, *J. Mater. Chem. A* **2**, 2942 (2014)
33. S.C. Yan, Z.S. Li, Z.G. Zou, *Langmuir* **25**, 10397 (2009)
34. L. Shi, L. Liang, F.X. Wang, J. Ma, J.M. Sun, *Catal. Sci. Technol.* **4**, 3235 (2014)
35. L. Shi, L. Liang, F.X. Wang, M.S. Liu, S.F. Zhong, J.M. Sun, *Catal. Commun.* **59**, 131 (2015)
36. F. Dong, L. Wu, Y. Sun, M. Fu, Z. Wu, S.C. Lee, *J. Mater. Chem.* **21**, 15171 (2011)
37. L. Shi, L. Liang, J. Ma, Y. Meng, S.F. Zhong, F.X. Wang, J.M. Sun, *Ceram. Int.* **40**, 3495 (2014)